Tree-ring oxygen isotope based inferences on winter and summer moisture dynamics over the glacier valleys of Central Himalaya

Nilendu Singh[1], Mayank Shekhar[2], Bikash Ranjan Parida[3], Anil K. Gupta[4], Kalachand Sain[1], Santosh K. Rai[1], Achim Bräuning[5], Vikram Sharma[6] and Reet Kamal Tiwari[7]

5 [1]*Wadia Institute of Himalayan Geology, Dehradun 248001, India*
  [2]*Birbal Sahni Institute of Palaeosciences, Lucknow 226007, India*
  [3]*Dept. of Geoinformatics, School of Natural Resource Management, Central University of Jharkhand, Ranchi 835222, India*
  [4]*Dept. of Geology and Geophysics, IIT Kharagpur, Kharagpur 721302, India*
  [5]*Institute of Geography, University of Erlangen–Nuremberg, 91058 Erlangen, Germany*
10 [6]*Banaras Hindu University, Varanasi 221005, India*
  [7]*Dept. of Civil Engineering, IIT Ropar 140001, India*

Correspondence to: Santosh K. Rai (*rksant@gmail.com*)

Abstract. Accelerated glacier mass loss is primarily attributed to greenhouse-induced warming, but land–climate interaction has increasingly been recognized as an important forcing at the regional-local scale. However, the related effects on the

15 Himalayan glaciers are less explored but believed to be an important factor regulating spatial heterogeneity. This study aims to present a multi-decadal approximation on hydroclimate and glacier interaction over the western central Himalaya (WCH). Three highly coherent, multi-species, tree-ring $\delta^{18}O$ site-chronologies from WCH were used to derive regional changes in atmospheric humidity (atmospheric moisture content: AMC) since the last four centuries. Coherency analyses between AMC and glacier mass balance (GMB: tree-ring $\delta^{13}C$-derived) indicate an abrupt phase-shift since the 1960s within a common

20 record of 273 years. To ascertain the cause of phase-shift, annual AMC was disintegrated into seasonal-scale, utilizing $\delta^{18}O$ record of deciduous species. Seasonal (winter: October–March; & summer-accumulation season: April–September) decomposition results reveal that winter-westerlies rather than summer precipitation from Indian summer monsoon (ISM) govern the ice-mass variability in WCH. Decadal coherency between summer-season AMC and GMB remained relatively stable since the mid-20th century, despite a decline in central Himalayan summer precipitation (tree-ring $\delta^{18}O$ records). We

25 hypothesize that excess water vapor brought to the atmosphere through increase in pre-monsoon precipitation and greening-mediated increase in evapotranspiration might have been recycled through the summer season to compensate for the ISM part of precipitation. However, isotope-enabled ecophysiological models and measurements would be able to strengthen this hypothesis. In addition, high-resolution radiative forcing and glacier valley-scale vegetation trend analyses point towards a probable influence of greening on GMB. Results indicate that attribution of ice-mass to large-scale dynamics is likely to be

30 modulated by local vegetation changes. We contend that glacier-climate models fed with these feedback processes could reliably improve the projections.

Climate
of the Past
Discussions

EGU

1   Introduction

Glaciers of the Himalaya–Karakoram–Tibetan Plateau (HKT) orogen sustain water resource for the downstream regions as well as it forms a region of perplexing hydroclimatic changes (Bonekamp et al., 2019; Fujita and Nuimura, 2011; Kapnick et
35   al., 2014; Sakai and Fujita, 2017; Wang et al., 2019; Yao et al., 2012, 2019). Primarily, the retreat and mass loss of the glaciers have been attributed to greenhouse warming. However, recent studies corroborate that local-regional forcing and feedback processes also play an important role over the glacierized valleys (de Kok et al., 2018, 2020; Lau et al., 2010; Managave et al., 2020; Pepin et al., 2015; Rashid et al., 2020; Sigdel et al., 2020; Yao et al., 2019). Several studies suggest that spatial heterogeneity in HKT is locally regulated by mechanisms associated with elevation-dependent warming, regional
40   land–climate interaction, and long-term variability in the atmospheric circulations (Kapncik et al., 2014; Lau et al., 2010; Managave et al., 2020; Mölg et al., 2012a, 2014, 2017; Pepin et al., 2015; Singh et al., 2020, 2021; Yao et al., 2019).
The climate heterogeneity in the Himalaya (Fig. 1) is even more pronounced. Such that many glaciers in Karakoram appear to be stable or advancing, while the glaciers in central Himalaya exhibit some of the fastest retreat rates (Bonekamp et al., 2019). Subjected to the geographical location, the Himalayan glaciers are known to be regulated by inter-decadal variability
45   in the winter-westerlies and the Indian summer monsoon (ISM) (Bookhagen and Burbank, 2010; Singh et al., 2021; Perry et al., 2020; Yao et al., 2019). However, recent studies on differential rates of heating and elevation-dependent warming have highlighted the importance of local land–climate interaction and feedback processes in ice-mass variability (Collier et al., 2013; de Kok et al., 2018, 2020; Lau et al., 2010; Mölg et al., 2012b; Pepin et al., 2015; Rashid et al., 2020; Sigdel et al., 2020; Yadav et al., 2019; Yao et al., 2019).
50   Satellite datasets (e.g., GPM, TRMM, etc.) and modelling efforts (High Asia Refined Analysis, APHRODITE) have been used for the climate heterogeneity analyses. However, these data-model integrations cannot be extended beyond a few decades and are too coarse to resolve regional-local changes. Further, inadequate understanding on regional land–climate interaction causes climate models to largely disagree on the projections (Watanabe et al., 2019; Jury et al., 2019). To improve coupled glacier-climate models, it is necessary to focus on important synthetic properties of local land–climate
55   interaction that are understood in a precise manner at one scale and could be extended to larger spatial and temporal scales without loss of information.
The tree-ring cellulose stable isotopes (particularly $\delta^{18}O$) provide such an unswerving source of century-scale hydroclimate variability, because of their inherent sensitivity to climate, coherence in the climatic response, and well understood environmental controls regulating tree physiology (Baker et al., 2016; Brunello et al., 2019; Huang et al., 2019; Levesque et
60   al., 2019; Sano et al., 2012, 2013, 2017; Singh et al., 2019, 2021; Treydte et al., 2001, 2006; Xu et al., 2017, 2018; Zeng et al., 2017).
In this study, we studied about three centuries of hydroclimate and glacier interaction over the western transition region of the central Himalaya (WCH) (Fig. 1). We synthesized three coherent tree-ring cellulose $\delta^{18}O$ site-chronologies of diverse tree species from different plant functional types, encompassing the last four centuries to derive regional changes in annual

Climate
of the Past
Discussions

65   and seasonal (winter and summer accumulation season) atmospheric moisture content (AMC). We utilized three centuries of glacier mass balance (GMB) data series derived from tree-ring cellulose carbon isotope ($\delta^{13}C$) chronologies of two conifer species growing in WCH glacier valleys (Singh et al., 2021). A set of information pertaining to the vegetation greening trends in the valleys, decadal changes in seasonal vegetation pattern, biophysical aspects and radiative fluxes were accessed using high-resolution satellite and CERES (Cloud and Earth Radiation Energy System) datasets. This study aims to

70   reconstruct annual and seasonal changes in AMC utilizing regional tree-ring $\delta^{18}O$ chronologies and to analyse its temporal coherence with GMB in relation with the local forcing factors.
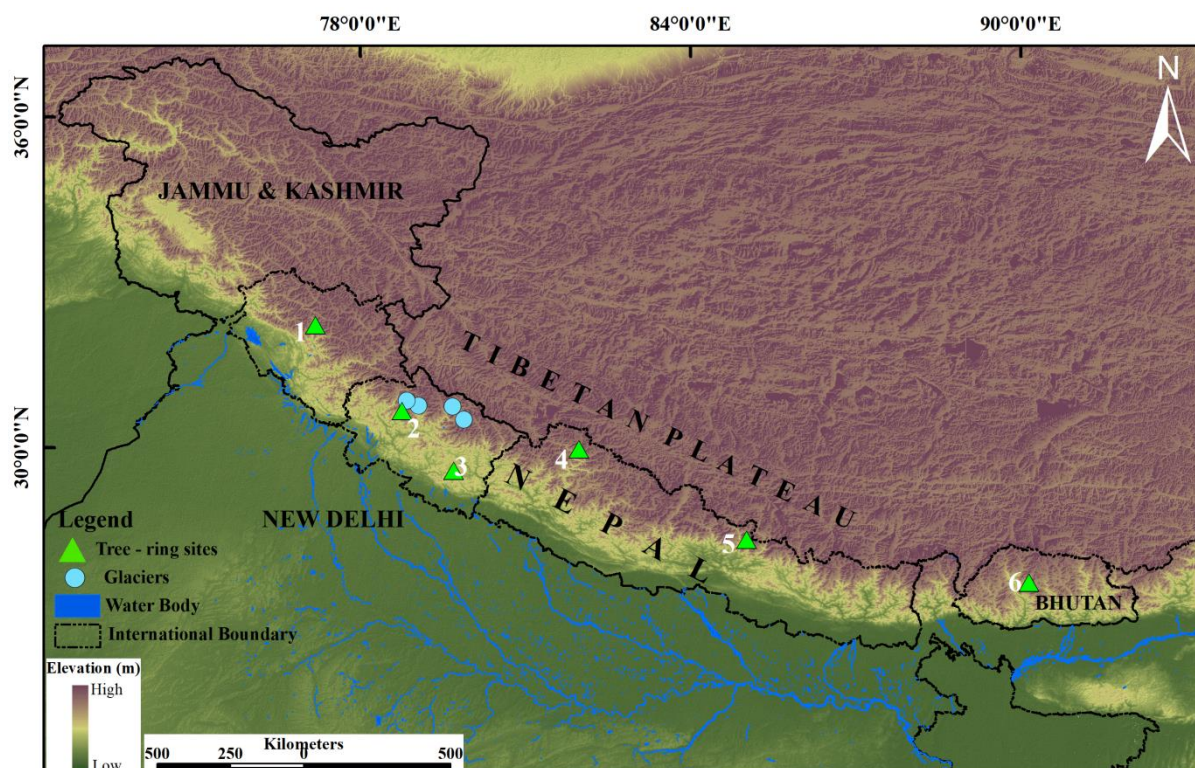

Figure 1. Study region showing the location of four benchmark glaciers (Blue circles: Dokriani Glacier, Chorabari Glacier, Tipra Bamak and Dunagiri Glacier) in the transitional western region of the central Himalaya (WCH). Green triangles indicate the location of tree-ring sites across the central Himalaya: (1) Manali (Sano et al., 2017), (2) Uttarakashi (Singh et al., 2019), (3) Jageshwar (Xu et al., 2018), (4) Humla (Sano et al., 2011), (5) Ganesh (Xu et al., 2018), and (6) Bhutan (Sano et al., 2013).

2   Materials and Methods

2.1 Study region and climate

75   The western transition region of the central Himalaya constitutes the study region (WCH: 29º 38' - 32º 13' N and 77º 13' - 80º 50' E) (Fig. 1). Glaciers in the region are fed by the ISM during summer and snow accumulation during winter is influenced by a precipitation regime driven by mid-latitude winter westerlies (Sano et al., 2012, 2017; Singh et al., 2019, 2021; Xu et al., 2018). Long-term meteorological records of higher reaches are limited and too are not readily available. Therefore, analyses of available regional records (CRU) indicate that annual precipitation is ~800 mm, of which the warm-

80   wet summer months (April-September) receive about 80%. Mean annual temperature varies around 5.5 °C, with a minimum (-9.4 °C) in January and a maximum (~18.5 °C) in July (Fig. S1). Tree-ring-derived century-scale hydro-climatological studies indicate a declining trend in precipitation derived from ISM in the region (Sano et al., 2012; 2017; Singh et al., 2019), while, the winter westerlies show an enhancement in recent decades (Treydte et al., 2006; Yadav et al., 2017). In contrast, tree-ring-derived regional temperature climatology show an increasing trend irrespective of the season, with a

85   prominent increase in winter temperatures (Gaire et al., 2020; Panthi et al., 2021; Shah et al., 2019).

2.2 Western Central Himalayan Tree-ring $\delta^{18}O$ records

Published tree-ring cellulose $\delta^{18}O$ records from three sites, distributed across the studied region (Fig. 1), comprising dominant tree species (Table 1) were used to reconstruct the climatology of regional atmospheric humidity (atmospheric moisture content: AMC). The first site (Manali: Sano et al., 2017) is located at the northwestern periphery of ISM incursions.

90   In the middle, $\delta^{18}O$ records from Uttarakashi (Singh et al., 2019) consisted of three species belonging to two different plant functional types (PFTs) that differ in the annual phenological cycle (Table 1). One PFT includes two evergreen conifers (*Abies pindrow* and *Picea smithiana*), while the other one was a dominant broadleaf deciduous species (*Aesculus indica*). Its growth period (April to September) coincides with warm-moist phase in the central Himalaya (thus lacks westerlies' signal during winter dormancy) (Singh et al., 2021). The isotopic record from the third site (Jageshwar: Xu et al., 2018) was the

95   longest (~ 400 years) and consisted of another dominant evergreen conifer (*Cedrus deodara*). Therefore, based on previous isotopic studies (Sano et al., 2017; Singh et al., 2019; Xu et al., 2018) and existing high annual correlation among tree-ring $\delta^{18}O$ records from WCH (Table 2), a ~ 400 year-long regional tree-ring $\delta^{18}O$ chronology was produced utilizing mean of above records.

2.3 Reanalysis datasets

100   Long-term meteorological records are available only for the lower elevations (< 2000 m asl). Therefore, gridded temperature and precipitation datasets for the study region were obtained from the Climatic Research Unit (CRU TS.3.22, 0.5˚ x 0.5˚, monthly, 1901-2015; Harris et al., 2014).

105 **Table 1**. Tree-ring oxygen isotope data sets of different tree species used in this study (WCH: western-central Himalaya; CH: Central Himalaya; ECH: eastern central Himalaya)

No.	Sampling site	Region and Coordinates	Tree species	Annual phenology	Period	Mean (±SD) ‰	Data source
1.	Manali	WCH: 32º13' N, 77º13' E;	*Abies pindrow*	Evergreen conifer	1768–2008	30.05 (± 1.48)	Sano et al., 2017
2.	Uttarakashi	WCH: 30º50' N, 78º43' E;	*Abies pindrow*	Evergreen conifer	1743–2015	29.44 (± 1.77)	
			Picea smithiana	Evergreen conifer	1830–2015	28.07 (± 1.68)	Singh et al., 2019
			Aesculus indica	Deciduous broadleaf (April-September)	1820–2015	25.74 (± 2.2)	
3.	Jageshwar	WCH: 29º38' N, 79º51' E;	*Cedrus deodara*	Evergreen conifer	1621–2008	29.68 (± 1.35)	Xu et al., 2018
4.	Humla	WCH: 29º51' N, 81º56' E;	*Abies spectabilis*	Evergreen conifer	1778–2000	25.16 (±1.67)	Sano et al., 2012
5.	Ganesh	CH: 28º10' N, 85º11' E;	*Abies spectabilis*	Evergreen conifer	1801–2000	22.26 (± 1.19)	Xu et al., 2018
6.	Bhutan	ECH: 27º59' N, 90º 00' E;	*Larix griffithii*	Deciduous conifer	1743–2011	19.24 (± 1.08)	Sano et al., 2013

Monthly reanalysis dataset of atmospheric moisture content (AMC; 0.5˚ x 0.625˚) was obtained from MERRA-2 (i.e., total precipitable water vapour, http://giovanni.sci.gsfc.nasa.gov) from 1982 to 2015 (n = 34 years). Soil moisture data were

110 obtained from the NOAA Climate Prediction Center (CPC) (0.5˚ x 0.5˚, monthly) (https://psl.noaa.gov/data/gridded/data.cpcsoil.html) during 1982-2015.

Table 2. Correlation between central Himalayan tree-ring $\delta^{18}O$ with three PFTs from Uttarakashi ($P < 0.05$)

Uttarakashi	Manali	Jageswar	Humla	Ganesh	Bhutan
(Singh et al., 2019)	(Sano et al., 2017)	(Xu et al., 2018)	(Sano et al., 2012)	(Xu et al., 2018)	(Sano et al., 2013)
Abies pindrow (Evergreen conifer)	0.75	0.67	0.23	0.20	0.26
Picea smithiana (Evergreen conifer)	0.69	0.56	0.50	0.52	0.26
Aesculus indica (Deciduous broadleaf)	0.60	0.55	0.50	0.57	0.31

2.4 Satellite-based observations

115 *MODIS*: Regional leaf area index (LAI: MOD15A2H) and evapotranspiration (ET: MOD16A2) was deduced using 500 m resolution, 8-day composite MODIS products since 2000 CE. Products were clipped using the shapefile for the studied region (WCH). Pixel values were then exported using ERDAS imagine to ASCII format. A MATLAB code was prepared to calculate average LAI value of each image. Overall, we followed processing manual for LAI and ET computations (www.reverb.echo.nasa.gov) (Table S1). Sensitivity of ET to LAI ($\Delta ET/\Delta LAI$) was derived as per Zeng et al. (2016).

120 *LANDSAT*: To detect changes in valley-scale vegetation area in the glacierized valleys of WCH (> 2500 m asl), we utilized 30 m resolution L1T Landsat data (a total of 766 images, Table S1) of different sensors onboard (MSS, TM, ETM+, OLI) since 1972 CE. In the study region, seasonal vegetation area of eight evenly distributed glacier valleys in WCH (Fig. 1, Table S2) were derived during summer (April-September: when both evergreen and deciduous canopy remain green) and during winter (October-March: evergreen species) from the NDVI (Normalized Difference Vegetation Index: > 0.3). The

125 images were downloaded (https://glovis.usgs.gov), processed and analyzed for the multi-year seasonal vegetation trends. Watershed boundary of each valley (Garhwal Himalaya: DOK, BHI, MAN and CHA Kumaun Himalaya: NAN, SUN, NAM and KAL; Table S2) was delineated utilizing mosaicked and re-projected tiles of 30 m Advanced Spaceborne Thermal Emission and Reflection Radiometer (ASTER) Global Digital Elevation Model (GDEM) v2 (http://gdex.-cr.usgs.gov/gdex/). Available L1T Landsat datasets with less than 10% cloud cover were selected and referenced to the Geographic Coordinate

130 system UTM Zone 44N. In order to bring time series data to a common scale, digital number values from each image were converted to radiance using gain and offset values specified in the image metadata. Selected Landsat images were transformed into NDVI time series using equation:

$$NDVI = \frac{NIR - Red}{NIR + Red}$$

Five-year seasonal image composite using the maximum value composite procedure was used, except for the period from

135 1972-1980, where nine-year composite was generated due to limited availability of cloud free images. Such compositing

Climate
of the Past

Discussions

EGU

process strongly reduces the effects of clouds, snow, seasonal differences caused by solar angle differences as well as the noise. While reducing the data volume, errors in phenological changes also get minimized.

CERES: Multi-year radiative forcing changes at the scale (Synoptic 1˚ x 1˚; monthly; Product: EBAF-TOA 4.0) of the eight glacierized valleys (Table S2) were observed with Cloud and Earth Radiation Energy System (CERES). It is one of the most

140   important global satellite detectors to monitor radiation and energy budget. Net radiative forcing and its components (shortwave and longwave), at the surface (SFA), and at the top of atmosphere (TOA) were downloaded from the official website (https://ceres.larc.nasa.gov/) at monthly scale from March 2000 to December 2018. Longwave, shortwave, and net fluxes under clear and all-sky conditions were used to compute radiative forcing at the TOA and SFA following the equations (1 to 9) given in Bao et al. (2019). Details of sensors and computation of radiation components are detailed in Bao

145   et al. (2019).

2.5 Glacier mass balance data

Present study utilizes tree-ring cellulose $\delta^{13}C$-derived 273 years of annual glacier mass balance reconstruction of four benchmark glaciers in the region (Singh et al., 2021). This reconstruction is based on previous and relevant glacio-hydrological studies (Borgoankar et al., 2009; Shekhar et al., 2017; Zhang et al., 2019). These four benchmark glaciers are

150   the longest monitored regional glaciers that are evenly distributed across the study region: Dokriani glacier (DOK in DOK valley), Chorabari glacier (CHO in MAN valley), Tipra Bamak (TIP in CHA valley) and Dunagiri glacier (DUN in NAN valley) (Fig. 1; Table S2).

2. 6 Statistical reconstruction and analyses

In a next step, and to understand the relationship between atmospheric humidity (AMC) and hydroclimatic signal in

155   evergreen conifers and broadleaf deciduous $\delta^{18}O$ data, simple Pearson correlations were applied with a response function approach. The confidence intervals of correlations were analyzed at 95 % and 99 % levels. This helped to investigate the correlations with monthly AMC averages in both the cases. The response function analysis in the case of evergreen conifers from August of the previous growth year through September of the current year revealed a highly significant correlation (r = -0.66; *P* < 0.001) (Fig. S2a). However, during peak winter, previous December and January showed a positive correlation

160   (Fig. S2a). Previously, positive correlation with winter atmospheric humidity has also been observed in the study region. However, correlations for these winter months were negative with the precipitation (Sano et al., 2012, 2017; Singh et al., 2019; Xu et al., 2018). A time lag induced by snowfall and winter frozen condition could be the plausible reason for this consistent behaviour across the study region. Therefore, to corroborate the response function with regional evergreen conifers, we also plotted three-month moving correlation coefficients between conifer $\delta^{18}O$ and mean AMC from 1982/1983

165   to 2014/2015). This considerably enhanced the correlations even for the winter months (Fig. S2b). In the case of broadleaf deciduous species having annual growth cycle between April and September, response function analysis showed a significant correlation (r = -0.63; *P* < 0.001) (Fig. S2c). Three-month moving correlation coefficients between deciduous

δ^{18}O and mean AMC substantially improved the relations (Fig. S2d). This is in parity and has been shown with three-month moving averages of leaf area index (LAI), correlation between evapotranspiration (ET) and LAI, and the sensitivity of ET to

170 LAI (ΔET/ΔLAI: mm day^{-1} (m^2 m^{-2})) (Fig. S2d).

Based on above significant correlations, we established linear regression models for AMC reconstructions: (1) for previous August to September based on δ^{18}O of regional conifers, and (2) for April to September based on δ^{18}O of broadleaf deciduous species (*Aesculus indica*). Reconstructions were performed using LM module in *R* (ggplot2 package, Wickham, 2016). Relevant statistics of calibration are shown in Table S3. In addition to usual statistics to check the strength of linear

175 regression model such as F-test, residual standard error, root mean square error, Durbin–Watson test, we applied Akaike's Information Criteria and Bayesian information criteria for model evaluation and selection (Table S3). Therefore, a linear regression model was employed for the reconstruction of annual (pAugust -September) AMC over the past 395 years (1621-2015), and the corresponding empirical equation is:

$$AMC_{annual} = 27.392 - 0.487 \times \delta 18O_{regional\ conifers}$$

180 Here, δ^{18}O$_{regional\ conifers}$ is the mean chronology regional evergreen conifers (Table 1) and AMC is annual atmospheric moisture content (Kg m^{-2}). Detailed calibration–verification statistics are presented in Table S3 and Fig. S3a, which indicate strength and the reliability of our reconstruction. Validation tests including the number of sign agreements between reconstructed series and observed mass balance records, and cross-correlation between reconstruction and measurements are significant ($P < 0.001$).

185 Furthermore, a linear regression model was also employed for the reconstruction of summer season (April - September) AMC over the past 196 years (1820-2015) utilizing δ^{18}O of a deciduous species (*Aesculus indica*). The corresponding empirical equation is:

$$AMC_{summer} = 25.885 - 0.388 \times \delta 18O_{deciduous}$$

Here, δ^{18}O$_{deciduous}$ is chronology of broadleaf deciduous species (*Aesculus indica*) and summer AMC is atmospheric moisture

190 content (Kg m^{-2}) during April to September. Corresponding model statistics are presented in Table S3. Model and calibration–verification statistics indicate reliability and strength of this reconstruction model (Table S3; Fig. S3b). Validation tests including the number of sign agreements between the reconstructed series and observed mass balance records, and cross-correlation between reconstruction and measurements are significant ($P < 0.001$) (Fig. S3). Finally, October to March AMC was estimated from above reconstructions.

195 The leave-one-out cross-validation method (LOOCV; Michaelsen, 1987) was used for the entire calibration period (1982/1983 – 2014/2015) and to verify the reconstruction (Table S3). This method is most suitable when the length of observed records is short (Shekhar et al., 2017; Singh et al., 2021; Zhang et al., 2019). In this method, each observation is successively withdrawn; a model is estimated on the remaining observations, and a prediction is made for the omitted observation. The LOOCV analysis was performed using package 'caret' (Kuhn et al., 2015). Statistics such as sign test,

200 product mean test (PMT), reduction of error (RE), and correlation coefficients were calculated to evaluate the similarity between observed and estimated values (Table S3; Fig. S3). The PMT and RE statistic provides a rigorous test of the

association between actual and estimated series. Positive value indicates the predictive capability of the model. A positive

RE is an evidence of a valid regression model (Fritts, 1976). In addition, other statistics, viz., root mean square error,

coefficient of efficiency, mean absolute error, and Durbin–Watson test were carried out to evaluate the linear regression

205   model (Table S3). The reconstructions were standardized using Z-scores and smoothed with 11-year or 21-year fast Fourier

transform to highlight the common climate signals.

3   Results and discussion

3.1 Coherent tree-ring δ¹⁸O site-chronologies of WCH

Tree-ring oxygen isotope ratio ($\delta^{18}O$) is a precise recorder of regional hydroclimatic condition (Baker et al., 2016). High

210   temporal coherency between site-chronologies expand the spatial scale and increases the reliability of dendroclimatic

reconstructions (Kahmen et al., 2011; Levesque et al., 2019; Managave et al., 2019; Sano et al., 2012, 2013, 2017; Singh et

al., 2021; Treydte et al., 2006; Xu et al., 2017, 2018; Zeng et al., 2017). Moreover, their climatic sensitivity enhances further,

when high correlations among site-chronologies allow the combination of tree species of diverse functional types (e.g.,

Singh et al., 2019). Over the HKT, cellulose $\delta^{18}O$ chronologies have been extensively utilized to study the spatial climate

215   heterogeneity extending over century to millennium-scale variability in regional hydroclimate, *viz.* changes in precipitation,

atmospheric moisture, cloud cover, vapor pressure, etc., (Grießinger et al., 2017; Huang et al., 2019; Hochreuther et al.,

2016; Managave et al., 2019; Sano et al., 2012, 2013, 2017; Singh et al., 2021; Treydte et al., 2006; Xu et al., 2018).

Over the central Himalaya, utilizing levels of correlations (0.11 – 0.94) among five tree-ring sites $\delta^{18}O$ chronologies, Xu et

al. (2018) showed a decline in the strength of ISM since the last 180 years. Moreover, utilizing $\delta^{18}O$ chronologies of two

220   different functional types (conifers and deciduous) from a WCH site (Uttarakashi), Singh et al. (2019) have confirmed a

declining summer precipitation in the region. These studies indicate that irrespective of sites and tree species, interannual

changes in ISM-derived atmospheric moisture is closely related to El Niño–Southern Oscillation, but correlation strength

varied synchronously across the central Himalaya (Sano et al., 2012, 2013, 2017; Singh et al., 2019; Xu et al., 2018).

However, our analyses of all the six published tree-ring $\delta^{18}O$ records across the central Himalaya (Table 1) show a

225   remarkable climatic distinction between the eastern (ECH) and the western central Himalaya (WCH) (Fig. S4). Studies even

have suggested increasing climate heterogeneity over the last six decades (Singh et al., 2021). Towards the eastern side, $\delta^{18}O$

records indicate normal ISM condition during the 20th century (Bhutan: Sano et al., 2013; Hochreuther et al., 2016). In

contrast, $\delta^{18}O$ chronologies from the central (Ganesh: Xu et al., 2018) and western part (WCH) (Manali: Sano et al., 2017;

Uttarakashi: Singh et al., 2019; Jageshwar: Xu et al., 2018; and Humla: Sano et al., 2012) unanimously show declining

230   summer monsoon precipitation (Fig. 2). Mean value of tree-ring $\delta^{18}O$ chronologies progressively decline eastwards (Fig.

S4), with a substantial difference (8-10 ‰) between Bhutan site (19.24 ‰) and WCH chronologies (29.31 ‰) (except

Humla) (Table 1). This difference probably indicates a lesser and a greater influence of the westerly circulation and the Bay

of Bengal branch of the ISM towards the eastern Himalaya (Perry et al., 2020; Sano et al., 2017; Singh et al., 2021). A

correlation matrix of six central Himalayan site chronologies (Table 2) indicates remarkably high correlations (0.55 – 0.75)

235   among the WCH chronologies (Manali: Sano et al., 2017; Uttarakashi: Singh et al., 2019 and Jageshwar: Xu et al., 2018).

However, an inclusion of the Humla $\delta^{18}O$ chronology (Sano et al., 2012) into WCH chronologies substantially lowers the

range of correlation (0.23 – 0.5) (Xu et al., 2018; Singh et al., 2019). Therefore, this study utilizes only the coherent WCH

chronologies for further analyses (Fig. 2). The WCH tree-ring $\delta^{18}O$ record spanning over the last four hundred years

indicates a prominent shift towards a drier phase after the 1960s. The recent drier phase in regional hydroclimate has

240   generally been attributed to anthropogenic emissions and resultant reduced land–ocean thermal contrasts (Xu et al., 2018).

Moreover, we found a strong correlation of WCH $\delta^{18}O$ values against evapotranspiration (ET, mm) ($R^2 = 0.48$, $P < 0.001$, n

= 15: 2000-2015) and atmospheric moisture content (AMC, Kg m^{-2}) ($R^2 = 0.38$, $P < 0.001$, n = 34: 1982-2015) as compared

to regional soil moisture (mm) ($R^2 = 0.13$, $P < 0.05$, n = 34: 1982-2015). These relationships points towards a dominant role

of the ecophysiology (stomatal control) in regulating atmospheric moisture (Kahmen et al., 2011; Singh et al., 2014). Earlier

245   studies (Baker et al., 2016) also found that in warm-moist tropical rainforest, $\delta^{18}O$ values are controlled by basin-intrinsic

ecophysiological processes. However, the mechanisms associated with physical fractionation of stable oxygen isotopes

indicates that tree-ring $\delta^{18}O$ values are mainly regulated by $\delta^{18}O$ of atmospheric moisture (Xu et al., 2018). Therefore, we

utilized coherent tree-ring $\delta^{18}O$ chronologies from WCH to reconstruct regional changes in annual AMC.
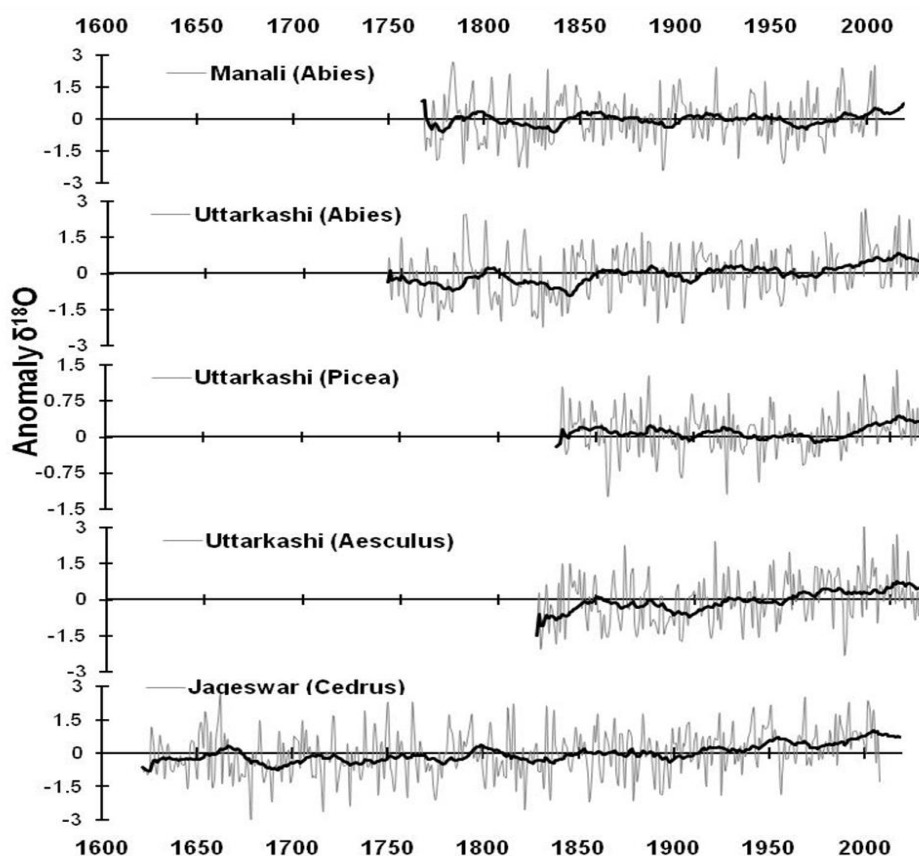
Climate
of the Past
Discussions

Figure 2. Anomalies (Z scores) of highly coherent site-chronologies from western central Himalaya (Manali: Sano et al., 2017; Uttarakashi: Singh et al., 2019; Jageshwar: Xu et al., 2018). Dark lines denote 21-year moving averages.

3.2 Regional atmospheric moisture content

250   The correlation ($r = -0.671$, $P < 0.001$, n = 34) between WCH $\delta^{18}O$ chronologies and observed AMC is strong enough to establish a significant calibration model. A linear regression model was thus employed for the reconstruction of annual AMC (pAugust - September) over the past 395 years (1621 – 2015). The equation accounts for 45 % of the AMC variance during the observation period (1982 – 2015). The model and calibration–verification statistics confirm the reliability of our reconstruction model. Validation tests including the number of sign agreements between reconstructed series and observed

255   AMC records, and cross-correlation between reconstruction and measurements were found to be significant ($P < 0.001$) (Table S3; Fig. S3a).

Smoothing of resultant annual AMC reconstruction with an 11-year moving average and break-point analyses indicates decreasing atmospheric moisture since the mid-19th century and a prominent decline in recent decades (since 1960s) (Fig. 3a). This result indicates that the ISM circulation is particularly responsible for the decline in the moisture influx in the

260   region (discussed later). Paleoclimatic evidence such as tree-ring $\delta^{18}O$ chronologies (Singh et al., 2019; Sano et al., 2012, 2013, 2017; Xu et al., 2018), speleothems (Kotlia et al., 2012; Liang et al., 2015) and ice-core records from the central Himalaya (Thompson et al., 2000; Kaspari et al., 2008) show that regional hydroclimate shifted towards a drier phase since the mid-19th century, and indicate towards a reorganisation of hemispheric atmospheric circulation following the Little Ice Age. Studies further attribute a recent decline in AMC (since 1960s) to increasing temperatures and an anthropogenic

265   climate change-induced decline in the ISM strength (Xu et al., 2018).

3.3 Reconstruction of seasonal atmospheric moisture content

About three hundred year-long glacier mass balance (GMB) variability record comprising four benchmark glaciers of WCH (Fig. 1) has previously been reconstructed utilizing cellulose $\delta^{13}C$ records of two regionally dominant evergreen conifer tree species (*Abies pindrow* and *Picea smithiana*) (Singh et al., 2021) (Fig. 3b). In this study, we plotted multi-decadal coherence

270   between GMB and AMC. Over the common record of 273 years, the 51-year moving correlations between atmospheric moisture and ice mass show a shift in the relationship since the mid-19th century, that became even more pronounced after the 1960s (Fig. 3c). To find the cause of this shift in AMC–GMB relationship, we decomposed the annual AMC into seasonal-scale (summer and winter accumulation seasons). AMC during the summer accumulation season (April – September) was derived based on a dominant deciduous tree species (*Aesculus indica*) that completes its annual phenological

275   cycle between April and September and remains completely dormant during winter (Singh et al., 2021). Approximately 200 years (1820 – 2015) of AMC record during the summer accumulation season was reconstructed based on a strong correlation

($r = -0.626$, $P < 0.001$, n = 34) with observed summer season AMC (1982 – 2015). The equation accounts for 39 % of the AMC variance during the observation period. The model calibration–verification and validation tests statistics indicate the reliability of the reconstruction (Table S3 and Fig S3b). In addition, winter season (October – March) AMC was derived
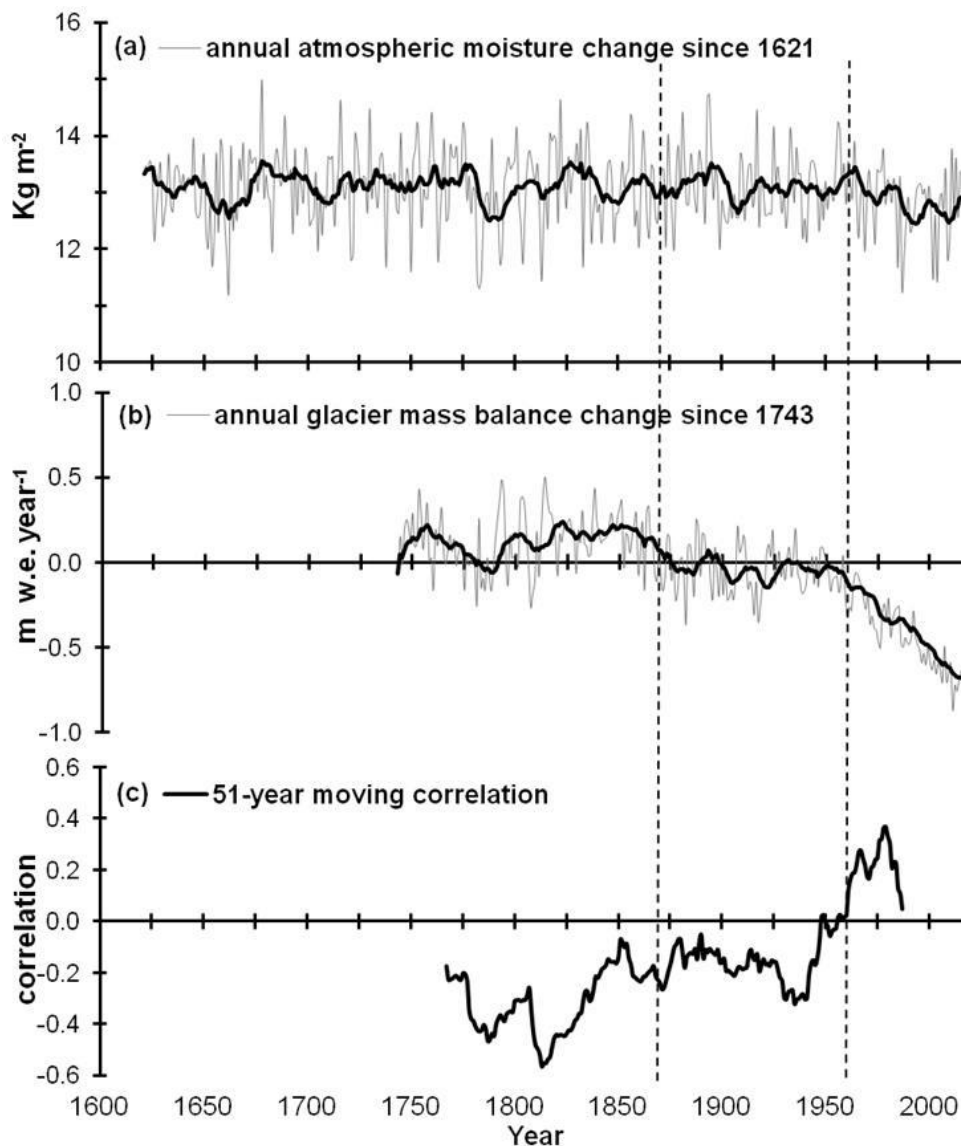
280 from annual AMC (Fig. 4).

Figure 3. (a) Annual (pAugust - September) AMC reconstruction derived from regional (WCH) conifer $\delta^{18}O$ chronologies (except deciduous species), (b) 273-years of glacier mass balance (GMB) variability reconstructed utilizing cellulose $\delta^{13}C$ records of WCH (Singh et al., 2021), and (c) Low-frequency temporal correlations (51-year running correlations) between annual AMC and GMB. Dark lines denote 11-year moving average. Vertical dashed lines are the results of break-point analysis.

Climate
of the Past
Discussions

3.3.1 Record of winter season atmospheric moisture content

In this study, we present a new reconstruction of AMC over the WCH during winter season (October – March), which provides baseline data from the western transitional region of the central Himalaya and an opportunity to assess its relationship with regional hydroclimatic records (such as precipitation, temperature, snowfall and river flow). Our record of about two centuries of winter season AMC indicates relatively stable condition prior to the 1920s, a period of decline between the 1920s and 1960s, and a revival of winter westerlies-driven moisture influx in the region since the 1970s (Fig. 4b). The reconstructed AMC shows a remarkable similarity with a tree-ring $\delta^{18}O$-derived millennium-scale precipitation record from the high mountains of northern Pakistan, where annual precipitation is dominated by westerly synoptic fronts (Treydte et al., 2006). Winter season AMC over WCH and precipitation in northern Pakistan showed a high inter-decadal coherence during the common period. The wet condition in the later part of the twentieth century is remarkably similar in both reconstructions. Similarly, Yadav et al. (2017) has also noted the moist condition since the 1970s in the Karakorum and the westerly-dominated Indian northwest Himalaya. They observed a decline in a tree-ring width-derived hydroclimatic index during early twentieth century, which is consistent with our AMC record (Yadav et al., 2017). A recent enhancement in moisture influx in the region from mid-latitude westerlies has been ascribed to the strengthening of western disturbance (Yadav et al., 2017), or possibly the anthropogenic influences on hydrological cycle acceleration (Treydte et al., 2006). In addition, several regional hydroclimatic records (precipitation, snowfall, river flow) substantiate our reconstruction (Bhutiyani et al., 2008, 2010; Cook et al., 2013; Singh and Yadav, 2013; Yadav and Bhutiyani, 2013). The decades of low AMC, viz., 1840s, 1870s, 1910-1920s and 1960-1970s, are consistent with the negative anomaly in regional hydroclimatic index (Yadav et al., 2017), low snowfall and flow in the Indus River (Cook et al., 2013; Yadav and Bhutiyani, 2013). River flow of the Indus and regional snowfall was relatively high in the 1890s, 1980s and 1990s when AMC was high in our reconstruction. The low AMC values recorded during 1960-1970s are consistent with low winter flow in the Satluj River (Bhutiyani et al., 2008; Singh and Yadav, 2013). The twentieth century low and high AMC episodes in our reconstruction have also been observed in instrumental winter precipitation and snowfall records from the western Himalaya (Bhutiyani et al., 2010; Yadav and Bhutiyani, 2013). The consistency in the decadal coherence between winter temperatures reconstructions from the central Himalaya (Gaire et al., 2020; Shah et al., 2019; Panthi et al., 2021) and our AMC records is remarkable, corroborating our results (Wang et al., 2020).

3.3.2 Record of summer season atmospheric moisture content

Similar to winter season AMC, our new record of summer-accumulation season (April to September) AMC is substantiated by regional hydroclimatic records. As discussed previously, summer season AMC ($r = -0.626$, $P < 0.001$, n = 34) is based on a regionally-dominant deciduous tree species (*Aesculus indica*). Related dendrochronological statistics (calibration–

verification and validation tests) indicate the strength of this reconstruction (Table S3 and Fig S3b). This record of about two

centuries of AMC indicates a consistent summer monsoon-driven moisture influx decline in the region at least from the

beginning of the 20th century. The result also underscores higher AMC levels during the 19th century, with some major

315   fluctuations (Fig. 4a). Broadly, all summer-monsoon season hydroclimatic records from the central Himalaya (Sano et al.,

2012, 2017; Xu et al., 2018; Singh et al., 2019) corroborate with our AMC reconstruction. Studies unanimously indicate a

weakening trend in the ISM circulation since the late 19th century or early 20th century (Singh et al., 2019). Even decadal to

inter-decadal pattern of our reconstructed series are consistent with available hydroclimatic records, e.g., the decades of low

summer season AMC, viz., 1840s and 1870s. Moreover, regional studies based on ice-cores and tree-ring $\delta^{18}O$ from the core

320   monsoon-zone of the Himalaya show a similar trend (Kaspari et al., 2008; Liu et al., 2013, 2014; Thompson et al., 2000;

Wernicke et al., 2017; Zhao and Moore, 2006). These records show a spatially coherent signal and serve as a validation test

of the accuracy of our AMC reconstruction. Particularly, tree-ring and speleothem $\delta^{18}O$ records (Singh et al., 2019, Sano et

al., 2012, 2017; Xu et al., 2018; Kotlia et al., 2012; Liang et al., 2015) from our study region appear consistent with our
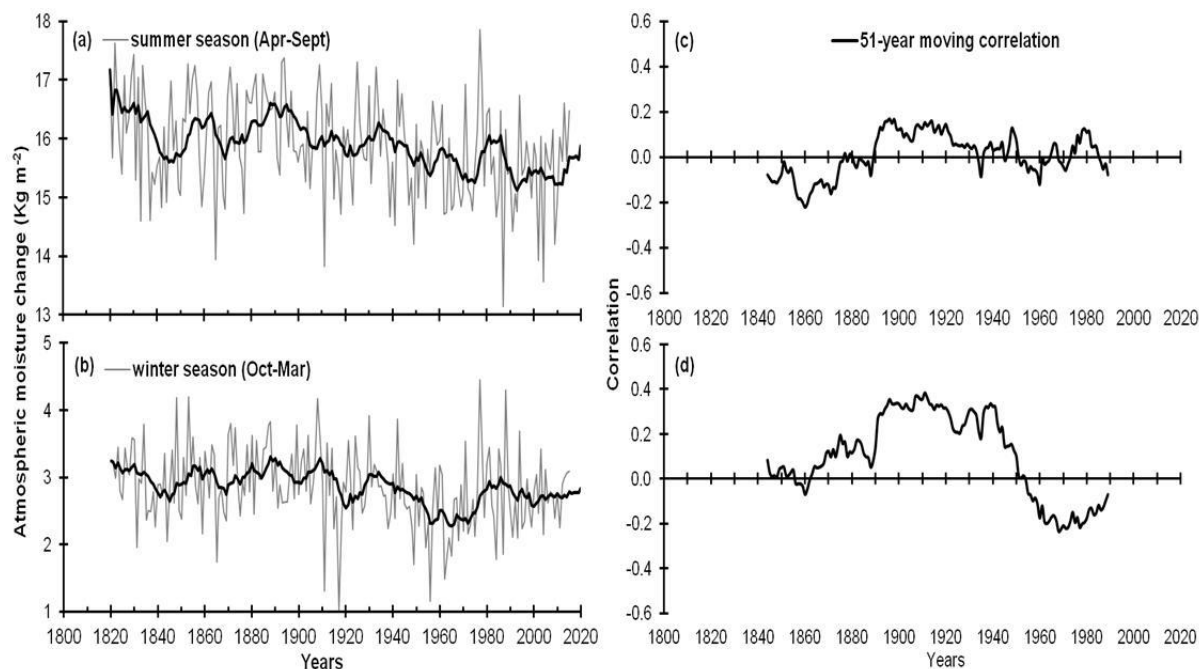
reconstruction.

Figure 4. (a) Summer season (April - September) AMC reconstruction derived from broadleaf deciduous
species(*Aesculus indica*), (b) Winter season AMC estimation based on annual and summer season AMC, (c-d)
Corresponding right panels indicate low-frequency temporal correlations (51-year running correlations) with
seasonal AMC.

325

3.4 Temporal correlation between ice mass and seasonal atmospheric moisture

3.4.1 Summer season AMC and glacier mass balance

The multi-decadal (51-year) moving correlations between annual GMB and summer-accumulation season AMC broadly indicate three phases in the common period (Fig. 4c). The correlations remained negative till the late 19th century, when our

330   result and available hydroclimatic records (Singh et al., 2019, Sano et al., 2012, 2017; Xu et al., 2018; Kotlia et al., 2012; Liang et al., 2015) indicated pluvial conditions. The correlations turned positive with a decline in summer moisture influx in the region since the 20th century (Fig. 4a). However, it is intriguing that despite a strong decline in summer precipitation since the mid-20th century (Fig. 2; Fig. 4a), correlations remained stable (Fig. 4c). Therefore, it is highly possible that increasing pre-monsoon precipitation in the region since the mid-20th century (Singh et al., 2006) might have compensated

335   for the ISM precipitation deficit that helped to lower down and maintain the correlation. Several studies confirm that the recent increase in pre-monsoon precipitation is consistently regional in nature (Karki et al., 2017; Shrestha et al., 2019; Talchabhadel et al., 2018). Higher temperatures increase the water holding capacity of the atmosphere according to the Clausius–Clapeyron relation, and further increase the evaporation from soil, glacial lakes, permafrost-active layer, snowmelt, and glacier runoff. Modelling studies have also found that October to March atmospheric moisture have a positive feedback

340   on ISM through large-scale circulation changes (Agarwal et al., 2019). Moreover, we comprehend that the reported decline in pre-monsoon surface temperature since the 1960s (Yadav et al., 2004) and concurrent increasing trend in pre-monsoon precipitation could be a consequence of evaporative cooling associated with regional vegetation greening (Shen et al., 2015). Multi-century temperature reconstructions from the adjacent western Nepal Himalayan region have also indicated that there is no increase in pre-monsoon temperature trends (Aryal et al., 2020; Thapa et al., 2015). In the Himalaya-Tibet orogen,

345   moisture recycling studies suggest a strong vegetation-precipitation feedback loop and high moisture recycling (Dirmeyer et al., 2009; Harding et al., 2013; Keys et al., 2016; Pathak et al., 2014; Tuinenburg et al., 2012). The isotopic moisture recycling studies in the orogen too have indicated high moisture recycling rates and an enhancement in trends in recent decades (An et al., 2017; Joswiak et al., 2013). Modelling experiments further confirm that vegetation-mediated moisture recycling is a major source of atmospheric water vapour and precipitation particularly during the pre-monsoon season, when

350   horizontal moisture transport is minimal.

3.4.2 Winter season AMC and glacier mass balance

Similar to the relationship for the summer season, moving correlations between GMB and winter season AMC revealed three phases in the common period of about two hundred years (Fig. 4d). Similarity even exists in the phase relationships. For example, during winter pluvial conditions prior to 1920s (Fig. 4b) (Treydte et al., 2006; Yadav et al., 2017), winter season

355   AMC and GMB correlations remained negative (Fig. 4d). During a brief stint of atmospheric moisture decline between 1920s and 1960s, the correlations significantly turned positive. With the revival of winter westerlies-driven moisture influx

in the region after the 1960s (Fig. 4b) (Treydte et al., 2006; Yadav et al., 2017), the correlations again tuned to negative (Fig. 4d). This behaviour probably indicates a high sensitivity of ice mass balance to the winter-westerlies in the region. In this context, it is increasingly being recognized that winter-westerlies primarily determine the ice mass variability at the decadal

360   timescales (Kumar et al., 2019; Singh et al, 2021). Therefore, we contend that caution should be applied when referring to the glaciers in WCH as predominantly ISM-fed or summer-accumulation type glaciers.

3.5 Vegetation greening and radiative balance analyses

Vegetation plays an important role modulating the radiative energy balance. Greening in recent decades has been influencing global surface energy partitioning, which is largely modulated by plant functional types (Forzieri et al., 2020; Lee and Lee,

365   2019; Zhu et al., 2016). In this context, the Himalaya is one of the largest global sources of vegetation-regulated moisture recycling. Isotopic studies and modelling experiments indicated a high moisture recycling rates and an enhancement in positive trend in recent decades (An et al., 2017; Dirmeyer et al., 2009; Keys et al., 2016; Harding et al., 2013; Tuinenburg et al., 2012). Moreover, strong seasonal coupling between the carbon and water cycle (Singh et al., 2014), ecohydrological memory (Chauhan and Ghosh, 2020), and a high interspecies and spatiotemporal coherence between tree-ring δ^{13}C and δ^{18}O

370   in WCH (Singh et al., 2021), indicates the existence of a strong land-atmosphere feedback (Singh et al., 2020). This confirms that vegetation-mediated moisture recycling is a significant source of atmospheric moisture and precipitation in the region. Therefore, the rate of greening (i.e., the rate of increase of LAI) and the rate of increase in evapotranspiration (ET) for the Himalaya, and particularly for the central Himalaya have been inferred utilizing MODIS products (500 m) (Table S2). Results over the Himalayan-scale indicate that during the last two decades (2000 - 2018), both LAI and ET have increased

375   by 16.7% and 12.5%, respectively ($P < 0.05$), with a high correlation between them (r = 0.787, $P < 0.001$). In the central Himalaya, the rates of increase in LAI (25.8 %) and ET (20.7 %) were significantly higher ($P < 0.001$) (Fig. S5), also showing a strong correlation (r = 0.736, $P < 0.001$). In addition, based on the significant and positive response of ET to greening, we derived sensitivity of ET to LAI (ΔET/ΔLAI) (Zeng et al., 2016) for the entire Himalaya and the central Himalaya. Constrained by the inversely proportional relation between (ΔET/ΔLAI) and the observed trend of LAI

380   (ΔLAI/Δt), Himalaya's sensitivity of ET to LAI was estimated at 1.26 mm d^{-1} per m^2 m^{-2}, which is almost four times higher than the global average ΔET/ΔLAI (Zeng et al., 2016). With this sensitivity, observed greening of the Himalaya is translated into acceleration of ET by a rate of ~35.3 mm yr^{-1}. Concerning the central Himalaya, it was equivalent at 32 mm yr^{-1}, corroborating previous studies that indicated the dominance of ET and recycled precipitation in local-regional precipitation climatology (deKok et al., 2018, 2020).

385   Further, we focussed on the glacier-valley region in WCH (Fig. 1) through high resolution MODIS (250 m) NDVI (> 0.3) (Table S2). Analyses (2000 - 2015) indicated a differential greening behaviour of the plant functional types. The deciduous vegetation coverage has expanded rapidly (37.2 km^2 yr^{-1}) with respect to the conifers, including evergreen vegetation (13.7 km^2 yr^{-1}) (Fig. S5). Thus, given annual phenology (April – September) of the deciduous species and probable repercussions

on atmospheric radiative balance (McPherson, 2007), five decades (1970 - 2016) of Landsat imageries (30 m) were further

390   utilized to ascertain the greening patterns and trends at glacier valley-scale (Table S2). Results corroborated a rapid increase in the deciduous vegetation with respect to the evergreen conifers (Fig. S7). On an average, deciduous vegetation coverage increased by 24% (15% – 35%) relative to the pre-1994 level across the WCH glacier-valleys. Current mean deciduous coverage area in the valleys is 36%, which varies between 22% and 49% in different glacier valleys. Both MODIS- and Landsat-derived seasonal green-area coverage analyses indicate that approximately 40% (range: 30% to 50%) of the valley

395   area rapidly turns-up green with deciduous canopy development (April – May) (Fig. S7). Numerous observations from the orogen have indicated a widespread greening and vegetation expansion including in the subnival vegetation (Anderson et al., 2020; Silva et al., 2016; Parida et al., 2020). Decadal-scale environmental changes resulting from atmospheric warming, augmented moisture and nutrient flow from snow-glacier melting, enhanced pre-monsoon rainfall, and disturbances such as forest fires might have favoured deciduous species' expansion. Thus, given widespread greening and thermophilization (a

400   preferential expansion of broadleaf deciduous vegetation over conifers), we contend comprehensive changes and a gross-scale alteration in surface–atmosphere interactions having direct implication on regional radiative balance. In addition, favoured expansion of deciduous vegetation on the valley slopes could even have repercussions on the seasonal radiative balance, as deciduous species remain leafless throughout the winter and rapidly turn-up green with the advent of the pre-monsoon season.

405   The above factors and associated changes in albedo, canopy conductance, aerodynamic properties and atmospheric moisture flux are expected to perturb the regional radiative balance. Therefore, CERES radiation dataset (2000 - 2018) covering glacier valleys in the WCH region were utilized to access shortwave (SRF), longwave (LRF) and net radiative forcing (NRF). Multi-year monthly average NRF at both the surface and at the top of atmosphere (TOA) showed unimodal annual behaviour (Fig. S8). NRF at TOA showed a maximum cooling effect (-45 to -55 W m^{-2}) during the monsoon months and

410   remained below -25 W m^{-2} during the rest of the months. Interestingly, surface NRF from October up to May (except monsoon months) indicate a heating effect or a feeble cooling (Fig. S8). Further, we performed seasonal-scale analyses (Fig. S8). During the post-monsoon to winter seasons, TOA NRF indicated a cooling effect (-5 and -20 W m^{-2}). In contrast, surface NRF indicated net heating (1.0 to 10 W m^{-2}). Similarly, during pre-monsoon, NRF at TOA remained between -10 and -30 W m^{-2}, while surface NRF indicated a weak cooling (0.6 and -14 W m^{-2}). However, with the advent of the monsoon,

415   both TOA and surface NRF resumed a cooling effect (Fig. S8). Annual SRF (at both surface and TOA) showed unimodal behaviour with a net cooling effect showing peak cooling (-70 to -100 W m^{-2}) during the monsoon months (Fig. S8). The magnitude (-15 and -50 W m^{-2}) of TOA and surface SRF remarkably deviated during winter to pre-monsoon seasons with a mean difference of 5 to 10 W m^{-2} (Fig. S8). Annually, LRF at both surface (38 W m^{-2}) and at TOA (24 W m^{-2}) had a heating effect (Fig. S8). Across the seasons, the magnitude of surface LRF varied slightly (monsoon: 30 W m^{-2}; winter to pre-

420   monsoon: 45 W m^{-2}). In contrast, LRF at TOA showed a unimodal behaviour with maximum heating (45 - 50 W m^{-2}) during the monsoon season and comparatively less heating (10 - 20 W m^{-2}) during winter to pre-monsoon seasons.

From the above results, particularly from radiative alterations during winter to pre-monsoon seasons, it is highly possible that enhanced winter precipitation (Fig. 3) coupled with winter warming (Gaire et al., 2020; Panthi et al., 2021; Shah et al., 2019) is making pre-monsoon environment more conducive for vegetation growth. Therefore, through vegetation-mediated
425   changes in albedo and roughness during the pre-monsoon season may have an immediate impact on regional radiation budget, which is manifested in atmospheric and surface radiative forcing. To conclude, the decline in surface albedo due to expanding valley forests, seasonal greening, increasing growing season length and tree-line advancement may act as a major determinant of radiative balance and ecohydrological feedbacks between valley forests, climate, and water resources.

4   Conclusions

430   Warming-induced acceleration in the hydrological cycle could have an immediate implication on regions with strong land-atmosphere coupling such as the Himalaya. In this study, we present the first tree-ring isotope-derived hydroclimate and glacier interaction over the western transitional climate region of the central Himalaya. We utilized highly coherent, multi-species tree-ring oxygen isotope chronologies to derive regional changes in atmospheric moisture since the last four centuries. Our reconstruction reveals decreasing atmospheric moisture since the mid-19th century and a prominent decline in
435   recent decades (since 1960s). Annual atmospheric moisture was further resolved into seasonal-scale utilizing an oxygen isotope record of a dominant broadleaf deciduous species. This helped to create a unique record of atmospheric moisture during the winter season (October – March) and a baseline data from this transitional climate zone. Our result testifies the revival of winter westerlies-driven moisture influx in the region since 1970s. Another reconstruction of about two centuries of atmospheric moisture during summer season (April - September) indicates a consistent decline in moisture influx from the
440   beginning of the 20th century. Low-frequency temporal correlations (51-year running correlations) between regional hydroclimate and ice mass balance indicate an abrupt phase-shift since the 1960s in a common record of 273 years. Our results specify that winter-westerlies rather than summer precipitation from ISM govern ice-mass variability in the WCH region. Radiative balance and glacier valley-scale vegetation analyses point towards a probable influence of greening on the ice mass balance. Our study contributes to the understanding of long-term hydroclimate – ice mass variability in the
445   Himalaya, where predictions are crucial for managing water resources and ecosystems. We suggest that fostering model representation of vegetation–atmosphere interactions with quantification of these feedback processes will ultimately enhance the reliability of future climate predictions.

Data and materials availability: Data needed to evaluate the conclusions are published, and presented in the paper and/or the Supplementary Material. Any additional data/code related to this paper may be requested from the authors.
450   **Author contributions**: N.S. analyzed final dataset and wrote first draft of the manuscript. M.S. performed reconstruction and respective analyses. All authors contributed equally to interpretation; discussion and editing of the manuscript.
Competing interests: All authors declare no competing interests.

Climate
of the Past
Discussions

References

Agrawal, S., Chakraborty, A., Karmakar, N., Moulds, S., Mijic, A. and Buytaert, W., 2019. Effects of winter and summer-
460   time irrigation over Gangetic Plain on the mean and intra-seasonal variability of Indian summer monsoon. *Climate Dynamics*, *53*(5-6), pp.3147-3166.

An, W., Hou, S., Zhang, Q., Zhang, W., Wu, S., Xu, H., Pang, H., Wang, Y. and Liu, Y., 2017. Enhanced recent local moisture recycling on the northwestern Tibetan Plateau deduced from ice core deuterium excess records. *Journal of Geophysical Research: Atmospheres*, *122*(23), pp.12-541.

465 Anderson, K., Fawcett, D., Cugulliere, A., Benford, S., Jones, D. and Leng, R., 2020. Vegetation expansion in the subnival Hindu Kush Himalaya. *Global Change Biology*, *26*(3), pp.1608-1625.

Aryal, S., Gaire, N.P., Pokhrel, N.R., Rana, P., Sharma, B., Kharal, D.K., Poudel, B.S., Dyola, N., Fan, Z.X., Grießinger, J. and Bräuning, A., 2020. Spring season in western Nepal Himalaya is not yet warming: a 400-year temperature reconstruction based on tree-ring widths of Himalayan Hemlock (Tsuga dumosa). *Atmosphere*, *11*(2), p.132.

470 Baker, J.C.A., Gloor, M., Spracklen, D.V., Arnold, S.R., Tindall, J.C., Clerici, S.J., Leng, M.J. and Brienen, R.J.W., 2016. What drives interannual variation in tree ring oxygen isotopes in the Amazon?. *Geophysical Research Letters*, *43*(22), pp.11-831.

Bao, S., Letu, H., Zhao, J., Lei, Y., Zhao, C., Li, J., Tana, G., Liu, C., Guo, E., Zhang, J. and He, J., 2020. Spatiotemporal distributions of cloud radiative forcing and response to cloud parameters over the Mongolian Plateau during 2003–
475   2017. *International Journal of Climatology*, *40*(9), pp.4082-4101.

Bhutiyani, M.R., Kale, V.S. and Pawar, N.J., 2008. Changing streamflow patterns in the rivers of northwestern Himalaya: implications of global warming in the 20th century. *Current Science*, pp.618-626.

Bhutiyani, M.R., Kale, V.S. and Pawar, N.J., 2010. Climate change and the precipitation variations in the northwestern Himalaya: 1866–2006. *International Journal of Climatology: A Journal of the Royal Meteorological Society*, *30*(4),
480   pp.535-548.

Bonekamp, P.N., de Kok, R.J., Collier, E. and Immerzeel, W.W., 2019. Contrasting meteorological drivers of the glacier mass balance between the Karakoram and central Himalaya. *Frontiers in Earth Science*, *7*, p.107.

Bookhagen, B. and Burbank, D.W., 2010. Toward a complete Himalayan hydrological budget: Spatiotemporal distribution of snowmelt and rainfall and their impact on river discharge. *Journal of Geophysical Research: Earth
485   Surface*, *115*(F3).

Borgaonkar, H.P., Ram, S. and Sikder, A.B., 2009. Assessment of tree-ring analysis of high-elevation Cedrus deodara D. Don from Western Himalaya (India) in relation to climate and glacier fluctuations. *Dendrochronologia*, *27*(1), pp.59-69.

Brunello, C.F., Andermann, C., Helle, G., Comiti, F., Tonon, G., Tiwari, A. and Hovius, N., 2019. Hydroclimatic seasonality
490   recorded by tree ring δ18O signature across a Himalayan altitudinal transect. *Earth and Planetary Science Letters*, *518*, pp.148-159.

Chauhan, T. and Ghosh, S., 2020. Partitioning of memory and real-time connections between variables in Himalayan ecohydrological process networks. *Journal of Hydrology*, *590*, p.125434.

Collier, E., Mölg, T., Maussion, F., Scherer, D., Mayer, C. and Bush, A.B.G., 2013. High-resolution interactive modelling of the mountain glacier-atmosphere interface: an application over the Karakoram. *The Cryosphere*, *7*(3), p.779.

Cook, E.R., Palmer, J.G., Ahmed, M., Woodhouse, C.A., Fenwick, P., Zafar, M.U., Wahab, M. and Khan, N., 2013. Five centuries of Upper Indus River flow from tree rings. *Journal of Hydrology*, *486*, pp.365-375.

de Kok, R.J., Tuinenburg, O.A., Bonekamp, P.N. and Immerzeel, W.W., 2018. Irrigation as a potential driver for anomalous glacier behavior in High Mountain Asia. *Geophysical research letters*, *45*(4), pp.2047-2054.

de Kok, R.J., Kraaijenbrink, P.D., Tuinenburg, O.A., Bonekamp, P.N. and Immerzeel, W.W., 2020. Towards understanding the pattern of glacier mass balances in High Mountain Asia using regional climatic modelling. *The Cryosphere*, *14*(9), pp.3215-3234.

Dirmeyer, P.A., Brubaker, K.L. and DelSole, T., 2009. Import and export of atmospheric water vapor between nations. *Journal of Hydrology*, *365*(1-2), pp.11-22.

Forzieri, G., Miralles, D.G., Ciais, P., Alkama, R., Ryu, Y., Duveiller, G., Zhang, K., Robertson, E., Kautz, M., Martens, B. and Jiang, C., 2020. Increased control of vegetation on global terrestrial energy fluxes. *Nature Climate Change*, *10*(4), pp.356-362.

Fritts, H. C.: Tree-Rings and Climate, Academic Press, London, 567, 1976.

Fujita, K. and Nuimura, T., 2011. Spatially heterogeneous wastage of Himalayan glaciers. *Proceedings of the National Academy of Sciences*, *108*(34), pp.14011-14014.

Grießinger, J.,Bräuning, A.,Helle, G., Hochreuther, P., Schleser, G. 2017. Late Holocene relative humidity history on the southeastern Tibetan plateau inferred from a tree-ring δ18O record: Recent decrease and conditions during the last 1500 years. *Quaternary International* 430: 52-59. DOI: 10.1016/j.quaint.2016.02.011.

Gaire, N.P., Fan, Z.X., Shah, S.K., Thapa, U.K. and Rokaya, M.B., 2020. Tree-ring record of winter temperature from Humla, Karnali, in central Himalaya: a 229 years-long perspective for recent warming trend. *Geografiska Annaler: Series A, Physical Geography*, pp.1-20.

Harding, R.J., Blyth, E.M., Tuinenburg, O.A. and Wiltshire, A., 2013. Land atmosphere feedbacks and their role in the water resources of the Ganges basin. *Science of the Total Environment*, *468*, pp.S85-S92.

Hochreuther, P., Wernicke, J., Grießinger, J., Mölg, T., Zhu, H., Wang, L. and Bräuning, A., 2016. Influence of the Indian Ocean Dipole on tree-ring δ 18 O of monsoonal Southeast Tibet. *Climatic Change*, *137*(1-2), pp.217-230.

Huang, R., Zhu, H., Liang, E., Grießinger, J., Wernicke, J., Yu, W., Hochreuther, P., Risi, C., Zeng, Y., Fremme, A. and Sodemann, H., 2019. Temperature signals in tree-ring oxygen isotope series from the northern slope of the Himalaya. *Earth and Planetary Science Letters*, *506*, pp.455-465.

Joswiak, D.R., Yao, T., Wu, G., Tian, L. and Xu, B., 2013. Ice-core evidence of westerly and monsoon moisture contributions in the central Tibetan Plateau. *Journal of Glaciology*, *59*(213), pp.56-66.

Jury, M.W., Mendlik, T., Tani, S., Truhetz, H., Maraun, D., Immerzeel, W.W. and Lutz, A.F., 2020. Climate projections for glacier change modelling over the Himalayas. *International Journal of Climatology*, *40*(3), pp.1738-1754.

Kahmen, A., Sachse, D., Arndt, S.K., Tu, K.P., Farrington, H., Vitousek, P.M. and Dawson, T.E., 2011. Cellulose δ18O is an index of leaf-to-air vapor pressure difference (VPD) in tropical plants. *Proceedings of the National Academy of Sciences*, *108*(5), pp.1981-1986.

Kapnick, S.B., Delworth, T.L., Ashfaq, M., Malyshev, S. and Milly, P.C., 2014. Snowfall less sensitive to warming in Karakoram than in Himalayas due to a unique seasonal cycle. *Nature Geoscience*, *7*(11), pp.834-840.

Kuhn, M., Wing, J., and Weston, S.: Package 'caret'. Classification and regression training. 2015

Karki, R., Schickhoff, U., Scholten, T. and Böhner, J., 2017. Rising precipitation extremes across Nepal. *Climate*, *5*(1), p.4.

535   Kaspari, S., Hooke, R.L., Mayewski, P.A., Kang, S., Hou, S. and Qin, D., 2008. Snow accumulation rate on Qomolangma (Mount Everest), Himalaya: synchroneity with sites across the Tibetan Plateau on 50–100 year timescales. *Journal of Glaciology*, *54*(185), pp.343-352.

Keys, P.W., Wang-Erlandsson, L. and Gordon, L.J., 2016. Revealing invisible water: moisture recycling as an ecosystem service. *PloS one*, *11*(3), p.e0151993.

540   Kotlia, B.S., Ahmad, S.M., Zhao, J.X., Raza, W., Collerson, K.D., Joshi, L.M. and Sanwal, J., 2012. Climatic fluctuations during the LIA and post-LIA in the Kumaun Lesser Himalaya, India: Evidence from a 400 y old stalagmite record. *Quaternary International*, *263*, pp.129-138.

Kumar, P., Saharwardi, M.S., Banerjee, A., Azam, M.F., Dubey, A.K. and Murtugudde, R., 2019. Snowfall Variability Dictates Glacier Mass Balance Variability in Himalaya-Karakoram. *Scientific Reports*, *9*(1), pp.1-9.

545   Lau, W.K., Kim, M.K., Kim, K.M. and Lee, W.S., 2010. Enhanced surface warming and accelerated snow melt in the Himalayas and Tibetan Plateau induced by absorbing aerosols. *Environmental Research Letters*, *5*(2), p.025204.

Lee, S. and Lee, M.I., 2019. Effects of surface vegetation on the intensity of East Asian summer monsoon as revealed by observation and model experiments. *International Journal of Climatology*, *40*(7), pp.3634-3648.

Levesque, M., Andreu-Hayles, L., Smith, W.K., Williams, A.P., Hobi, M.L., Allred, B.W. and Pederson, N., 2019. Tree-ring
550   isotopes capture interannual vegetation productivity dynamics at the biome scale. *Nature Communications*, *10*(1), pp.1-10.

Liang, F., Brook, G.A., Kotlia, B.S., Railsback, L.B., Hardt, B., Cheng, H., Edwards, R.L. and Kandasamy, S., 2015. Panigarh cave stalagmite evidence of climate change in the Indian Central Himalaya since AD 1256: Monsoon breaks and winter southern jet depressions. *Quaternary Science Reviews*, *124*, pp.145-161.

555   Liu, X., Xu, G., Grießinger, J., An, W., Wang, W., Zeng, X., Wu, G. and Qin, D., 2014. A shift in cloud cover over the southeastern Tibetan Plateau since 1600: evidence from regional tree-ring δ18O and its linkages to tropical oceans. *Quaternary Science Reviews*, *88*, pp.55-68.

Liu, X., Zeng, X., Leavitt, S.W., Wang, W., An, W., Xu, G., Sun, W., Wang, Y., Qin, D. and Ren, J., 2013. A 400-year tree-ring δ18O chronology for the southeastern Tibetan Plateau: Implications for inferring variations of the regional
560   hydroclimate. *Global and Planetary Change*, *104*, pp.23-33.

Managave, S., Shimla, P., Yadav, R.R., Ramesh, R. and Balakrishnan, S., 2020. Contrasting Centennial-Scale Climate Variability in High Mountain Asia Revealed by a Tree-Ring Oxygen Isotope Record From Lahaul-Spiti. *Geophysical Research Letters*, *47*(4), p.e2019GL086170.

Mölg, T., Maussion, F., Yang, W. and Scherer, D., 2012a. The footprint of Asian monsoon dynamics in the mass and energy
565   balance of a Tibetan glacier. *The Cryosphere*, *6*(6), pp.1445-1461.

Mölg, T., Großhauser, M., Hemp, A., Hofer, M. and Marzeion, B., 2012b. Limited forcing of glacier loss through land-cover change on Kilimanjaro. *Nature Climate Change*, *2*(4), pp.254-258.

Mölg, T., Maussion, F. and Scherer, D., 2014. Mid-latitude westerlies as a driver of glacier variability in monsoonal High Asia. *Nature Climate Change*, *4*(1), pp.68-73.

570   Mölg, T., Maussion, F., Collier, E., Chiang, J.C. and Scherer, D., 2017. Prominent midlatitude circulation signature in High Asia's surface climate during monsoon. *Journal of Geophysical Research: Atmospheres*, *122*(23), pp.12-702.

Panthi, S., Fan, Z.X. and Bräuning, A., Ring widths of Rhododendron shrubs reveal a persistent winter warming in the central Himalaya. *Dendrochronologia*, *65*, p.125799.

Pathak, A., Ghosh, S. and Kumar, P., 2014. Precipitation recycling in the Indian subcontinent during summer
575   monsoon. *Journal of Hydrometeorology*, *15*(5), pp.2050-2066.

Parida, B.R., Pandey, A.C. and Patel, N.R., 2020. Greening and browning trends of vegetation in India and their responses to climatic and non-climatic drivers. *Climate*, *8*(8), p.92.

Climate
of the Past
Discussions

Pepin, N., Bradley, R.S., Diaz, H.F., Baraër, M., Caceres, E.B., Forsythe, N., Fowler, H., Greenwood, G., Hashmi, M.Z., Liu, X.D. and Miller, J.R., 2015. Elevation-dependent warming in mountain regions of the world. *Nature climate*
580   *change*, *5*(5), pp.424-430.

Perry, L.B., Matthews, T., Guy, H., Koch, I., Khadka, A., Elmore, A.C., Shrestha, D., Tuladhar, S., Baidya, S.K., Maharjan, S. and Wagnon, P., 2020. Precipitation characteristics and moisture source regions on Mt. Everest in the Khumbu, Nepal. *One Earth*, *3*(5), pp.594-607.

Rashid, I., Majeed, U., Aneaus, S. and Pelto, M., 2020. Linking the Recent Glacier Retreat and Depleting Streamflow
585   Patterns with Land System Changes in Kashmir Himalaya, India. *Water*, *12*(4), p.1168.

Sakai, A. and Fujita, K., 2017. Contrasting glacier responses to recent climate change in high-mountain Asia. *Scientific Reports*, *7*(1), pp.1-8.

Sano, M., Dimri, A.P., Ramesh, R., Xu, C., Li, Z. and Nakatsuka, T., 2017. Moisture source signals preserved in a 242-year tree-ring δ18O chronology in the western Himalaya. *Global and Planetary Change*, *157*, pp.73-82.

590   Sano, M., Ramesh, R., Sheshshayee, M.S. and Sukumar, R., 2012. Increasing aridity over the past 223 years in the Nepal Himalaya inferred from a tree-ring δ18O chronology. *The Holocene*, *22*(7), pp.809-817.

Sano, M., Tshering, P., Komori, J., Fujita, K., Xu, C. and Nakatsuka, T., 2013. May–September precipitation in the Bhutan Himalaya since 1743 as reconstructed from tree ring cellulose δ18O. *Journal of Geophysical Research: Atmospheres*, *118*(15), pp.8399-8410.

595   Shah, S.K., Pandey, U., Mehrotra, N., Wiles, G.C. and Chandra, R., 2019. A winter temperature reconstruction for the Lidder Valley, Kashmir, Northwest Himalaya based on tree-rings of Pinus wallichiana. *Climate Dynamics*, *53*(7-8), pp.4059-4075.

Shekhar, M., Bhardwaj, A., Singh, S., Ranhotra, P.S., Bhattacharyya, A., Pal, A.K., Roy, I., Martín-Torres, F.J. and Zorzano, M.P., 2017. Himalayan glaciers experienced significant mass loss during later phases of little ice age. *Scientific*
600   *reports*, *7*(1), pp.1-14.

Shen, M., Piao, S., Jeong, S.J., Zhou, L., Zeng, Z., Ciais, P., Chen, D., Huang, M., Jin, C.S., Li, L.Z. and Li, Y., 2015. Evaporative cooling over the Tibetan Plateau induced by vegetation growth. *Proceedings of the National Academy of Sciences*, *112*(30), pp.9299-9304.

Shrestha, S., Yao, T. and Adhikari, T.R., 2019. Analysis of rainfall trends of two complex mountain river basins on the
605   southern slopes of the Central Himalayas. *Atmospheric Research*, *215*, pp.99-115.

Sigdel, S.R., Zhang, H., Zhu, H., Muhammad, S. and Liang, E., 2020. Retreating Glacier and Advancing Forest Over the Past 200 Years in the Central Himalayas. *Journal of Geophysical Research: Biogeosciences*, *125*(9), p.e2020JG005751.

Silva, L.C., Sun, G., Zhu-Barker, X., Liang, Q., Wu, N. and Horwath, W.R., 2016. Tree growth acceleration and expansion
610   of alpine forests: The synergistic effect of atmospheric and edaphic change. *Science Advances*, *2*(8), p.e1501302.

Singh, J. and Yadav, R.R., 2013. Tree-ring-based seven century long flow records of Satluj River, western Himalaya, India. *Quaternary International*, *304*, pp.156-162.

Singh, J., Park, W.K. and Yadav, R.R., 2006. Tree-ring-based hydrological records for western Himalaya, India, since AD 1560. *Climate Dynamics*, *26*(2-3), pp.295-303.

615   Singh, J., Singh, N., Chauhan, P., Yadav, R.R., Bräuning, A., Mayr, C. and Rastogi, T., 2019. Tree-ring δ18O records of abating June–July monsoon rainfall over the Himalayan region in the last 273 years. *Quaternary International*, *532*, pp.48-56.

Singh, N., Patel, N.R., Bhattacharya, B.K., Soni, P., Parida, B.R. and Parihar, J.S., 2014. Analyzing the dynamics and inter-linkages of carbon and water fluxes in subtropical pine (Pinus roxburghii) ecosystem. *Agricultural and Forest*
620   *Meteorology*, *197*, pp.206-218.

Climate
of the Past

Discussions

Singh, N., Shekhar, M., Singh, J., Gupta, A.K., Bräuning, A., Mayr, C. and Singhal, M., 2021. Central Himalayan tree-ring isotopes reveal increasing regional heterogeneity and enhancement in ice mass loss since the 1960s. *The Cryosphere*, *15*(1), pp.95-112.

Singh, N., Singhal, M., Chhikara, S., Karakoti, I., Chauhan, P. and Dobhal, D.P., 2020. Radiation and energy balance dynamics over a rapidly receding glacier in the central Himalaya. *International Journal of Climatology*, *40*(1), pp.400-420.

Talchabhadel, R., Karki, R., Thapa, B.R., Maharjan, M. and Parajuli, B., 2018. Spatio-temporal variability of extreme precipitation in Nepal. *International Journal of Climatology*, *38*(11), pp.4296-4313.

Thapa, U.K., Shah, S.K., Gaire, N.P. and Bhuju, D.R., 2015. Spring temperatures in the far-western Nepal Himalaya since AD 1640 reconstructed from Picea smithiana tree-ring widths. *Climate dynamics*, *45*(7-8), pp.2069-2081.

Thompson, L.G., Yao, T., Mosley-Thompson, E., Davis, M.E., Henderson, K.A. and Lin, P.N., 2000. A high-resolution millennial record of the South Asian monsoon from Himalayan ice cores. *Science*, *289*(5486), pp.1916-1919.

Treydte, K., Schleser, G.H., Schweingruber, F.H. and Winiger, M., 2001. The climatic significance of δ13C in subalpine spruces (Lötschental, Swiss Alps) a case study with respect to altitude, exposure and soil moisture. *Tellus B*, *53*(5), pp.593-611.

Treydte, K.S., Schleser, G.H., Helle, G., Frank, D.C., Winiger, M., Haug, G.H. and Esper, J., 2006. The twentieth century was the wettest period in northern Pakistan over the past millennium. *Nature*, *440*(7088), pp.1179-1182.

Tuinenburg, O.A., Hutjes, R.W.A. and Kabat, P., 2012. The fate of evaporated water from the Ganges basin. *Journal of Geophysical Research: Atmospheres*, *117*(D1).

Wang, J., Yang, B. and Ljungqvist, F.C., 2020. Moisture and temperature covariability over the Southeastern Tibetan Plateau during the Past Nine Centuries. *Journal of Climate*, *33*(15), pp.6583-6598.

Wang, R., Liu, S., Shangguan, D., Radić, V. and Zhang, Y., 2019. Spatial heterogeneity in glacier mass-balance sensitivity across High Mountain Asia. *Water*, *11*(4), p.776.

Watanabe, M., Yanagawa, A., Watanabe, S., Hirabayashi, Y. and Kanae, S., 2019. Quantifying the range of future glacier mass change projections caused by differences among observed past-climate datasets. *Climate Dynamics*, *53*(3-4), pp.2425-2435.

Wernicke, J., Hochreuther, P., Grießinger, J., Zhu, H., Wang, L. and Bräuning, A., 2017. Multi-century humidity reconstructions from the southeastern Tibetan Plateau inferred from tree-ring δ18O. *Global and Planetary Change*, *149*, pp.26-35.

Wickham, H. ggplot2: elegant graphics for data analysis. Springer, 2016.

Xu, C., Sano, M., Dimri, A.P., Ramesh, R., Nakatsuka, T., Shi, F. and Guo, Z., 2018. Decreasing Indian summer monsoon on the northern Indian sub-continent during the last 180 years: evidence from five tree-ring cellulose oxygen isotope chronologies. *Climate of the Past*, *14*(5).

Xu, C., Shao, X., An, W., Nakatsuka, T., Zhang, Y., Sano, M. and Guo, Z., 2017. Negligible local-factor influences on tree ring cellulose δ 18O of Qilian juniper in the Animaqing Mountains of the eastern Tibetan Plateau. *Tellus B: Chemical and Physical Meteorology*, *69*(1), p.1391663.

Yadav, J.S., Pratap, B., Gupta, A.K., Dobhal, D.P., Yadav, R.B.S. and Tiwari, S.K., 2019. Spatio-temporal variability of near-surface air temperature in the Dokriani glacier catchment (DGC), central Himalaya. *Theoretical and Applied Climatology*, *136*(3-4), pp.1513-1532.

Yadav, R.R. and Bhutiyani, M.R., 2013. Tree-ring-based snowfall record for cold arid western Himalaya, India since AD 1460. *Journal of Geophysical Research: Atmospheres*, *118*(14), pp.7516-7522.

Yadav, R.R., Gupta, A.K., Kotlia, B.S., Singh, V., Misra, K.G., Yadava, A.K. and Singh, A.K., 2017. Recent wetting and glacier expansion in the northwest Himalaya and Karakoram. *Scientific Reports*, *7*(1), pp.1-8.

Yadav, R.R., Park, W.K., Singh, J. and Dubey, B., 2004. Do the western Himalayas defy global warming?. *Geophysical Research Letters*, *31*(17).

Yang, W., Guo, X., Yao, T., Zhu, M. and Wang, Y., 2016. Recent accelerating mass loss of southeast Tibetan glaciers and the relationship with changes in macroscale atmospheric circulations. *Climate Dynamics*, *47*(3-4), pp.805-815.

Yao, T., Thompson, L., Yang, W., Yu, W., Gao, Y., Guo, X., Yang, X., Duan, K., Zhao, H., Xu, B. and Pu, J., 2012. Different glacier status with atmospheric circulations in Tibetan Plateau and surroundings. *Nature Climate Change*, *2*(9), pp.663-667.

Yao, T., Xue, Y., Chen, D., Chen, F., Thompson, L., Cui, P., Koike, T., Lau, W.K.M., Lettenmaier, D., Mosbrugger, V. and Zhang, R., 2019. Recent third pole's rapid warming accompanies cryospheric melt and water cycle intensification and interactions between monsoon and environment: Multidisciplinary approach with observations, modeling, and analysis. *Bulletin of the American Meteorological Society*, *100*(3), pp.423-444.

Zeng, X., Liu, X., Treydte, K., Evans, M.N., Wang, W., An, W., Sun, W., Xu, G., Wu, G. and Zhang, X., 2017. Climate signals in tree-ring δ18O and δ13C from southeastern Tibet: insights from observations and forward modelling of intra-to interdecadal variability. *New Phytologist*, *216*(4), pp.1104-1118.

Zeng, Z., Zhu, Z., Lian, X., Li, L.Z., Chen, A., He, X. and Piao, S., 2016. Responses of land evapotranspiration to Earth's greening in CMIP5 Earth System Models. *Environmental Research Letters*, *11*(10), p.104006.

Zhang, R., Wei, W., Shang, H., Yu, S., Gou, X., Qin, L., Bolatov, K. and Mambetov, B.T., 2019. A tree ring-based record of annual mass balance changes for the TS. Tuyuksuyskiy Glacier and its linkages to climate change in the Tianshan Mountains. *Quaternary Science Reviews*, *205*, pp.10-21.

Zhao, H. and Moore, G.W.K., 2006. Reduction in Himalayan snow accumulation and weakening of the trade winds over the Pacific since the 1840s. *Geophysical Research Letters*, *33*(17).

Zhu, Z., Piao, S., Myneni, R.B., Huang, M., Zeng, Z., Canadell, J.G., Ciais, P., Sitch, S., Friedlingstein, P., Arneth, A. and Cao, C., 2016. Greening of the Earth and its drivers. *Nature Climate Change*, *6*(8), pp.791-795.